

An Alternate Pathway for H_2 Formation in the Early Universe:

A physical process to account for the presence and
coevolution of the luminous galaxies and supermassive
black holes at the high redshifts

Amrendra Pandey, Olivier Dulieu and Nadia Bouloufa-Maafa
Laboratoire Aimé Cotton, Université Paris-Saclay, CNRS, Orsay, 91405,
Orsay, France.

*Corresponding author(s). E-mail(s):
amrendra.pandey@universite-paris-saclay.fr;
Contributing authors: olivier.dulieu@cnrs.fr;
nadia.bouloufa@universite-paris-saclay.fr;

Abstract

Molecular hydrogen (H_2) and hydrogen deuteride (HD) are key coolants in primordial gas and regulate the formation of the first stars and proto-galaxies. Recent results from the James Webb Space Telescope provide striking insights into galaxies detected at high redshifts, which are found to be significantly more abundant and luminous than expected from galaxy formation models, thus suggesting a gap in our understanding of the early Universe. Standard pathways for H_2 formation in the early Universe proceed through the H^- and H_2^+ intermediates, both of which are strongly suppressed at high redshift by the cosmic microwave background. We propose an additional pathway for H_2 and HD formation that could be active as early as the end of the epoch of recombination and could enable the formation of the first stars earlier than the current prediction at redshift $z \simeq 30 - 20$. The proposed pathway relies on the manifestation of Jahn-Teller dynamical coupling between electronic states of H_3^+ . This coupling induces transient three-body recombination in H^+ , H and H, and charge exchange within the charged atom-dimer complex ($\text{H}+\text{H}_2^+$ or H^++H_2) that directly creates ground-state H_2 (and HD), bypassing the fragile intermediates that limit the standard primordial pathways. Our analysis

shows that this mechanism could occur under the thermodynamic conditions of the post-recombination epoch, also suggesting that it might be playing a role in the active galactic nuclei feedback processes, regulating the formation rates of the first stars and the accretion rates of the first black holes. Though the global impact on galaxy formation and black-hole growth is not yet determined and will require quantitative assessment in future modeling, the mechanism offers an additional chemical route for H_2 and HD formation, with substantial cosmological relevance for primordial chemistry and early structure formation.

Keywords: H_2 chemistry, Jahn-Teller coupling, Three-Body Recombination, Charge Exchange, JWST, The Early Universe, Pop III stars, Supermassive Black Holes, galaxy-SMBH co-evolution

1 Introduction

Understanding the formation of the first stars is a central issue in modern astrophysics and cosmology¹⁻³. In the standard cold dark matter model, the first generation of stars, known as Population III (Pop III), formed from primordial, metal-free gas in the early Universe at redshifts $z \simeq 30 - 20$. These stars emerged inside dark matter minihalos with typical masses of $\sim 10^6 M_\odot$ (M_\odot is the solar mass) and virial temperatures of order 1,000 K²⁻⁶. Star formation in such environments requires the collapsing gas to cool efficiently. This condition is captured by the Rees-Ostriker-Silk criterion, which specifies when the radiative cooling in a dark matter minihalo is sufficient to allow gas fragmentation and the onset of star formation, marking the beginning of galactic evolution³. From the end of the recombination era ($z \sim 1100$), through the Dark Ages, and into the epoch of reionization (down to $z \sim 6$), cooling in the absence of heavy elements depended almost entirely on molecular hydrogen (H_2)^{7,8}. Consequently, the chemical evolution of H_2 played a decisive role in controlling the thermal state of the gas and the formation of the first stars^{5,9}.

Current cosmological models indicate that the Big Bang nucleosynthesis created mostly ^1H ($\sim 75\%$) and ^4He ($\sim 25\%$), as well as about 0.01% of ^2D and ^3He , and a trace fraction consisting of other light elements, such as lithium and beryllium. Before the epoch of reionization, cooling at $\sim 10^4$ K was mediated by atomic H. At lower temperatures, the gas cooled through H_2 with cooling rate that scales roughly linearly with its fraction and the excitation energy of its lowest rovibrational transition, reaching a minimum temperature ~ 200 K at a density of $n_{\text{H}} \sim 10^4 \text{ cm}^{-3}$ (Pop III.1 formation pathway)⁵. Numerical simulations based on the primordial H_2 chemistry and the associated cooling and heating processes suggest that the first stars were massive ($\gtrsim 100 M_\odot$) and short-lived ($\sim \text{few Myr}$)²⁻⁵. In conditions where the HD population increases, the primordial gas can cool even further via HD, reaching temperatures of approximately 50-100 K at a density of $n_{\text{H}} \sim 10^6 \text{ cm}^{-3}$. This enhanced cooling enables the formation of relatively low-mass stars ($\gtrsim 1-10 M_\odot$ with lifetimes

of ~ 10 s Myr) in dark matter mini-halos that are smaller by about an order of magnitude compared to those associated with H_2 -dominated cooling (Pop III.2 formation pathway)⁵. The intrinsic distinction between these two scenarios is that HD can cool the gas via the dipole-allowed rotational transition $J_{\text{HD}} = 1 \rightarrow 0$ with lower excitation energy of $\simeq 128$ K, whereas H_2 cooling relies on the much slower quadrupole rotational transition $J_{\text{H}_2} = 2 \rightarrow 0$ with an excitation energy of $\simeq 512$ K.

James Webb Space Telescope (JWST) observations have revealed very luminous galaxies at Cosmic Dawn ($z > 10$), pointing to extremely rapid galaxy formation^{10–15}. Spectroscopically confirmed objects such as JADES-GS-z14-0 ($z \approx 14$)¹² and MoM-z14 ($z = 14.44$)¹⁴ show that luminous galaxies already existed less than 300 million years after the Big Bang, with an abundance well above pre-JWST expectations. Several other sources (e.g., GN-z11¹⁰, GHZ2/GLASS-z12¹³) exhibit unusual chemical abundance patterns, including elevated N/O ratios, suggesting enrichment dominated by very massive stars. The detection of [O III] 88 μm emission in JADES-GS-z14-0¹⁶ further indicates early oxygen enrichment of the interstellar medium. Other studies,¹⁷ report massive, dust-obscured galaxies at $z = 5 - 9$ with baryon-to-stellar conversion efficiencies approaching $\sim 50\%$, far higher than those inferred for the most efficient systems at later epochs. In addition, candidate galaxies at $z \approx 17 - 25$ ¹⁸, if spectroscopically confirmed, would imply even more extreme early growth, which will be difficult to reconcile with standard galaxy-formation models. Potential explanations include enhanced star-formation efficiency or strong dust attenuation, a top-heavy initial mass function, or contributions from active galactic nuclei^{19–21}. Furthermore, observations of spiral galaxies such as ceers-2112²², Big Wheel²³, and Alaknanda²⁴ from the first two billion years of the Universe challenge traditional models of galaxy evolution. In short, along with the observation of luminous galaxies at $z > 10$ and their earlier chemical enrichment, the presence of supermassive black holes in the first few billion years of the Universe^{25–29}, detection of the large scale structures like spiral and bar formation in the early galaxies suggests towards the timeline shift of the star formation, more efficient stellar and cosmic structure evolution.

In the era before the Cosmic Dawn ($z > 10$), molecular hydrogen existed only in trace amounts. Its relative abundance, $x_{\text{H}_2} (= n_{\text{H}_2}/n_{\text{H}})$, was approximately 10^{-6} until $z \sim 100$, and eventually reaching 10^{-3} by $z \simeq 30 - 20$, primarily due to H^- ⁸ and H_2^+ ⁷ mechanisms in collapsing dark matter minihalos^{3,5}. Both H^- and H_2^+ mechanisms are two-step reactions and are limited at high redshifts. In cosmological simulations, the H^- mechanism dominates at redshifts of $z \simeq 30 - 20$, when the first stars formed³⁰. A third process, i.e., three-body reaction among three neutral hydrogen atoms, becomes important at high particle densities above $\sim 10^9 \text{ cm}^{-3}$ ^{5,9}. These reactions and their coupling with other trace atomic species in the early Universe have been widely studied^{9,30}. Today ($z = 0$), H_2 mainly forms by the grain surface catalytic process ($\text{H} + \text{H} + \text{surface} \rightarrow \text{H}_2 + \text{surface}$)³¹.

In this work, we propose a new reaction pathway that produces neutral H_2 and HD in their ground electronic states. Based on a previous study of the ion-atom-atom rubidium system³², the formation results from transient three-body recombination (TTBR) and charge exchange (CE) occurring on Jahn-Teller-induced (JT-induced) conical intersections³³ in a pair of singlet H_3^+ states of colliding H^+ , $\text{H}(1s)$, and $\text{H}(1s)$

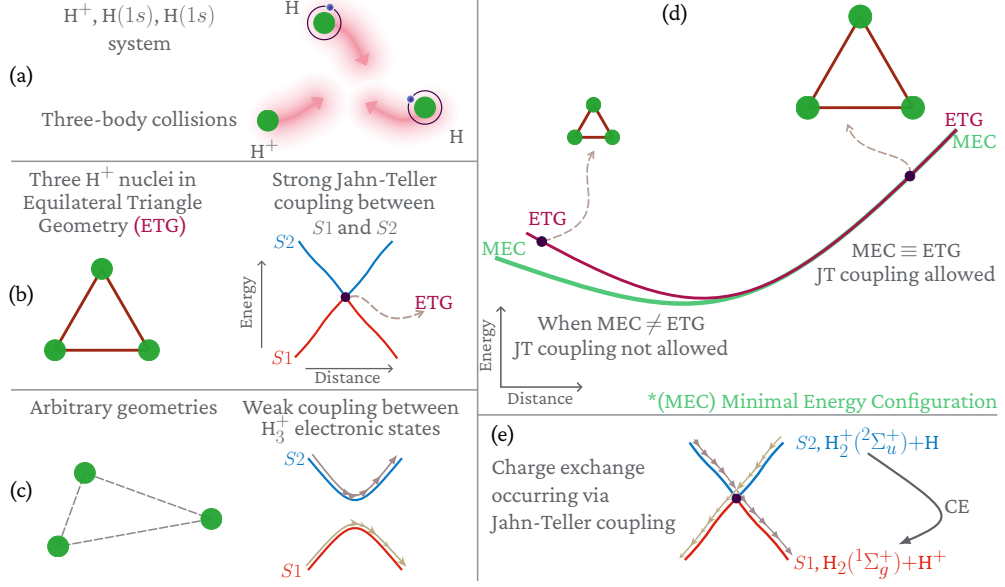


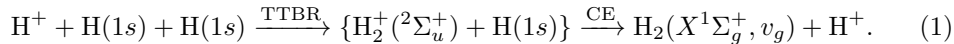
Fig. 1 | Jahn-Teller coupling in H_3^+ states. (a) Schematic diagram of two hydrogen atoms, $H(1s)$, and a H^+ ion, interacting in a three-body collision via Coulomb forces. (b) Equilateral triangle geometry (ETG) for three H^+ nuclei along with the cuts to the two singlet potential energy surfaces (PESs) of the two-electron H_3^+ system, S_1 and S_2 , depicted as functions of the internuclear separation, varying from left to right. In a collision, when the nuclei reach an ETG, the two singlet surfaces S_1 and S_2 cross each other through Jahn-Teller coupling. (c) At the geometries other than ETGs, S_1 and S_2 usually don't intersect, preventing curve-crossing reactions. The grey arrows on top of S_1 and S_2 represent movements of the nuclei guided by the PESs. (d) Two cuts to a PES of H_3^+ . The curve labeled ETG represents the seam of the JT-coupled singlet states where S_1 and S_2 are degenerate. The other curve depicts the potential energies along the minimal energy configuration (MEC) and is representative of the geometries accessed by the colliding H^+ , $H(1s)$, and $H(1s)$. JT coupling will be accessed in collisions only in the region where MEC is identical to the ETG, satisfying the primary constraint for the JT-induced reaction, i.e., TTBR and CE. (e) The possibility of CE is further controlled by the requirement that S_1 and S_2 be reciprocally associated with H_2^+ and H_2 dimers.

triads. This proposed mechanism likely influences the formation rates of H_2 and HD in the early Universe, with consequences for the onset and efficiency of structure formation and subsequent evolution.

2 A new reaction pathway for H_2 and HD formation

For homonuclear triatomic molecules like H_3^+ , the collective nuclear Coulomb field of the high-symmetry equilateral triangle geometry (ETG), belonging to the D_{3h} point group, leads to intersections in its electronic states, often termed symmetry-required conical intersections. Jahn-Teller-induced conical intersections are ubiquitous to these triatomic molecules and have been studied for many alkali neutral and ionic species³². For H_3^+ , out of three singlet and three triplet electronic states associated with the first fully atomized asymptotic limit, $H^+ + H(1s) + H(1s)$, a pair of singlet states, $2^1A'$

and $3^1A'$, and a pair of triplet states, $1^3A'$ and $2^3A'$, exhibit Jahn-Teller conical intersections at the ETGs for all interparticle separations. JT coupling in the singlet states of H_3^+ , namely $2^1A'$ (as $S1$) and $3^1A'$ (as $S2$), is shown using a few schematic diagrams in Fig. 1 (a) - (c). H_2 formation via the JT-induced TTBR+CE mechanism in $S1$ and $S2$ states involves JT-induced transient three-body recombination (TTBR) among ion-atom-atom $H^+ + H(1s) + H(1s)$, and JT-induced charge exchange (CE) of the transition state $\{H_2^+(^2\Sigma_u^+) + H(1s)\}$ to neutral $H_2(X^1\Sigma_g^+)$ and H^+ ,



The requirement for the JT-induced TTBR is illustrated in Fig. 1 (d): i.e., JT coupling between $S1$ and $S2$ will be accessed in collisions only in the region where the electronic potential energy for the minimal energy configuration (MEC) is identical to the one for ETGs. JT-induced CE requires one more condition to be fulfilled: i.e., the curves $S1$ and $S2$ must be reciprocally associated with H_2^+ and H_2 dimers (as illustrated in Fig. 1 (e)). These arguments are developed in Methods (see details in section 5.2) and include the necessary discussion of the computation of H_3^+ potential energy surfaces (PESs). The role of the participants' initial kinetic energies is also discussed in Methods (see details in section 5.4). In addition to H_2 , the JT-induced TTBR+CE mechanism would also produce HD when the reaction occurs among $H^+ + H(1s) + D(1s)$ complex, given that under the Born-Oppenheimer approximation the PESs of H_3^+ and H_2D^+ are identical.

Since both JT-induced TTBR and CE reactions involve $S1$ and $S2$ H_3^+ states, they can occur in a single collision. This is a crucial difference from the two standard pathways for primordial H_2 formation (via H^- and H_2^+ intermediates), as they are two-step processes. Their initial steps, namely the radiative attachment forming H^- and the radiative association forming H_2^+ , are highly susceptible to destruction through photodetachment of H^- or photodissociation of H_2^+ by the intense thermal cosmic microwave background (CMB) radiation and by non-thermal recombination photons in the Wien tail^{30,34}. For this reason, both are limited at high redshift. H_2 production peaks at $z \sim 260$ for the H_2^+ mechanism and at $z \sim 90$ for the H^- mechanism³⁰. In contrast, once H_2 in the ground electronic state $X^1\Sigma_g^+(v_g)$ is produced, it is relatively robust—the CMB and non-thermal photons are too weak at post-recombination redshifts to excite H_2 to the Lyman-Werner (LW) bands, making its photodissociation negligible³⁰. Uniquely, as the proposed JT-induced TTBR+CE mechanism forms ground-state H_2 directly in a single step, it bypasses the fragile H^- and H_2^+ intermediates (further details in section 5.3). Because this pathway relies on non-adiabatic couplings and rapid transitions near conical intersections, known to be efficient in molecular formation^{35,36}, it is likely to provide an additional H_2 formation route under primordial conditions where the conventional channels are strongly suppressed. For instance, in the high H-density conditions with considerable H^+ , i.e., at the end of the epoch of recombination ($z \sim 1100$), in the outflows of the active galactic nuclei (AGNs) hosting black holes, and in star-forming collapsing dark matter minihalos, the H_2 fraction likely rises significantly from the JT-induced TTBR+CE reactions. While the overall cosmological impact remains to be quantitatively assessed, this mechanism

is expected to be active in the post-recombination epoch. As a promising trend, the motivation for the present study is rooted in our earlier investigations of heavier ion-atom-atom systems $\text{Rb}^+ + \text{Rb} + \text{Rb}$ ³², where explicit inclusion of Jahn-Teller coupling was shown to resolve apparently contradictory experimental observations of three-body recombination reactions. In those systems, the JT-induced mechanism provided a unified explanation for the simultaneous production of weakly bound ionic dimers and deeply bound neutral dimers, while reproducing experimentally observed reaction rates that could not be accounted for within conventional semi-classical three-body recombination models. These results demonstrate that Jahn-Teller coupling can qualitatively drive three-body collision dynamics and open efficient reaction pathways that would otherwise be inaccessible. Building on this insight, the present work extends the same conceptual framework to the prototypical and astrophysically most relevant system, i.e., $\text{H}^+ + \text{H}(1s) + \text{H}(1s)$.

Additionally, Jahn-Teller couplings in the excited manifolds of H_3^{+*} imply that reaction channels analogous to the TTBR+CE process in ground-state $\text{H}^+ + \text{H}(1s) + \text{H}(1s)$ can also operate when one or more H atoms are in excited states. These pathways can produce excited H_2^* , which subsequently relaxes to the ground electronic state through radiative or non-radiative processes, thereby contributing to H_2 formation in environments where a significant fraction of hydrogen resides in excited levels. Such conditions may arise in astrophysical environments characterized by strong radiation fields or dense photoionized gas. For instance, some AGNs show Balmer line absorption features (e.g., H_α , H_β), indicating the presence of $\text{H}(n = 2)$ in their line-of-sight gas^{37–42}, and thus demonstrating the existence of pockets of excited atomic hydrogen under the high-energy conditions near accreting supermassive black holes. Our results suggest that, if efficient, JT-induced TTBR+CE pathways for excited H_3^{+*} manifolds could constitute an additional route for H_2 formation in localized regions of AGN outflows or irradiated gas. The enhanced cooling may, therefore, accelerate galactic growth further once the proto-galaxy has developed a central black hole. Observational evidence shows that AGN-driven winds can contain or generate molecular material^{43,44}, and some studies suggest that molecules may form in situ within these outflows⁴⁵. Considering these astrophysical environments, our alternate pathway promises to have a significant impact on the star formation processes in the early Universe.

3 Early structure formation, the first stars and black holes

The JT-induced TTBR+CE mechanism implies an enhancement in H_2 and HD fractions at early times, thereby modifying the cooling properties of gas within collapsing halos and, consequently, the characteristic mass scale of the first stars and black holes. Specifically, in the extreme scenario where there is efficient production of HD at the end of the epoch of recombination ($z \sim 1100$), this would suggest a rapid stellar development at a very early stage. The smaller characteristic excitation energy of HD (~ 128 K) compared to H_2 (~ 512 K), and the resulting lower virial temperature (T_{vir}) of cooling gas, imply a lowering of the mass of dark-matter minihalos ($M \propto (T_{vir}/(z+1))^{3/2}$)^{1,46} by about an order of magnitude compared to the H_2 -dominated

cooling-based Pop III.1 star formation pathway; for instance, from $M \sim 10^6 M_\odot$ to $\sim 10^5 M_\odot$. Consequently, for the HD-dominated cooled primordial gas, the smaller dark-matter minihalos will be assembled at the earlier time at redshift $z \sim 50$, instead of the typical case of Pop III.1 formation pathway at $z \approx 30 - 20$ ⁴⁷. As a result, it could provide an additional ~ 100 Myr for galactic evolution, substantially increasing current theoretical estimates that rely on the Pop III.1 formation pathway for the first stars.

Considering the synopsis of early formation of the first stars, efficient cooling from additional H_2 and HD would also influence the creation and growth of the first black holes (BHs) in proto-galaxies. Over the past decades, luminous quasars, powered by accretion onto supermassive black holes (SMBHs) with masses around $10^9 M_\odot$ at high redshifts ($z > 6$), have been observed. Additionally, JWST has detected fainter SMBHs at even higher redshifts, with masses in the range $10^6 - 10^8 M_\odot$. The presence of these objects in the early Universe has been challenging to understand²⁵⁻²⁹. Many scenarios for the formation of the first BHs and the growth mechanisms for SMBHs have been proposed. Black hole seed models include light seeds from $\sim 100 M_\odot$ Pop III.1 remnants at $z \gtrsim 20$ ⁴⁸, intermediate-mass seeds formed via stellar collisions or black hole mergers in dense clusters²⁶, and heavy seeds produced as $\sim 10^5 - 10^6 M_\odot$ direct-collapse black holes (DCBHs) from metal-free gas cooled only through atomic H in $\sim 10^8 M_\odot$ dark matter halos with virial temperatures above 10^4 K²⁶. Despite extensive study, no consensus exists²⁹. Light-seed scenarios rely on sustained super-Eddington accretion⁴⁹, which is disfavored by AGN feedback and star formation activities⁵⁰, while intermediate-mass and direct-collapse seeds appear too rare in simulations to explain the observed abundance of SMBHs⁵¹.

Efficient cooling and rapid fragmentation—caused by increased H_2 and HD production in the early Universe—undermine heavy-seed DCBH models. These models require suppression of molecular cooling to prevent gas fragmentation^{26,28}. Therefore, they consider the presence of intense LW irradiation, which would destroy the built-up H_2 population^{26,28}. On the contrary, if LW photons are present, they would also excite $H(n = 2, 3, \dots)$ and promote H_2 formation through H_3^{+*} excited states, thereby further reducing the likelihood of direct collapse scenarios.

In contrast, efficient molecular cooling will raise interstellar gas density and enhance accretion, potentially reaching super-Eddington rates^{26,28}. Therefore, the increased H_2 and HD generated by the JT-induced TTBR+CE mechanism favor the formation of light-seed BHs and support their sustained growth by facilitating the accretion of dense, efficiently cooled stellar matter. H_2 and HD production from excited H_3^{+*} states may also help drive accretion in the first high-redshift AGNs³⁷⁻⁴². Moreover, the timeline shift of the first stars, and consequently, the first black holes, possibly to redshift range $30 < z < 50$ (from the upper limit of Pop III.1 formation case to the proposed scenario of JT-induced TTBR+CE HD-dominated cooling), provides additional time up to ~ 100 Myr for growth, reducing the strain on the required accretion rates. Observations of super-Eddington accretion in the high-redshift BHs and quasars^{52,53}, along with various extreme accretion scenarios⁴⁹, show support for rapid growth in the early Universe. Recent studies of moderate- and low-mass high-redshift AGNs (e.g., Maiolino *et al.* at $4 < z < 11$ (with $M_{BH} \sim 10^7 - 10^5 M_\odot$)³⁸, Geris

et al. at $3 < z < 7$ with $M_{\text{BH}} \sim 10^6 M_{\odot}$ ⁵⁴, CAPERS-LRD-z9 AGN at $z = 9.288$ of mass $> 10^7 M_{\odot}$ ⁴⁰, and currently the furthest SMBH in GN-z11 at $z = 10.6$ with mass of $\sim 1.6 \times 10^6 M_{\odot}$ ⁵⁵) consider accretion-driven growth of light-seed BHs as a viable pathway. This route becomes even more compelling in the presence of the JT-induced TTBR+CE mechanism.

4 BH-galaxy coevolution and AGN feedback

As we previously discussed, AGN outflows will likely accelerate H_2 and HD production via the ground and excited manifolds of H_3^+ . The accelerated cooling by AGN outflows, therefore, may positively regulate both the star formation rates in the host galaxy and the accretion rate of central SMBHs. As a result, AGN feedback acting as a cooling agent could drive the well-established BH-galaxy coevolution, such as the linear positive correlation between the mass of SMBHs, M_{BH} , and the stellar mass of their host galaxies, M_{\star} ^{42,56}. Since AGN feedback influences the large-scale structures by processes such as extreme radiation pressure, accretion disc winds, and jets, it has been considered one of the possible candidates for regulating the coevolution, although its complete role remains unresolved^{41,42}. Observations of AGNs with high accretion rates, often found in gas-rich, star-forming galaxies, further support the role of the feedback⁴². In the presence of JT-induced TTBR+CE mechanism, AGN-driven H_2 production in the host galaxy and the interstellar medium provides a candidate for the physical channel responsible for the BH-galaxy coevolution. Interestingly, recent JWST observations of low-luminosity and low-mass AGNs/BHs at higher redshift suggest that some early black holes may lie above the local $M_{\text{BH}}-M_{\star}$ relation, potentially indicating rapid early BH growth relative to their host galaxies.^{38,54,55} For example, AGNs at $4 < z < 11$ ($M_{\text{BH}} \sim 10^7 - 10^5 M_{\odot}$) and at $3 < z < 7$ ($M_{\text{BH}} \sim 10^6 M_{\odot}$), reported by Maiolino *et al.*^{38,55} and Geris *et al.*⁵⁴, respectively. The present mechanism also suggests that BH growth in the early Universe would precede the rate of star formation when both are regulated by AGN feedback, aligning with these JWST-detected AGNs at higher redshifts.

In conclusion, we propose a new pathway for molecular hydrogen (H_2) and hydrogen deuterium (HD) formation in the early Universe, driven by Jahn-Teller-induced transient three-body recombination and charge exchange in the H_3^+ system. Unlike the standard H^- and H_2^+ channels, which are strongly suppressed at high redshift by the CMB, this mechanism directly forms ground-state H_2 and HD in a single collision. By bypassing fragile intermediates, it may operate efficiently under post-recombination conditions. Enhanced H_2 and HD abundances would significantly improve primordial gas cooling, enabling earlier and more efficient fragmentation in low-mass dark matter minihalos, thus shifting the onset of Population III star formation to higher redshifts than predicted by standard models. The resulting acceleration of stellar evolution would provide additional time for the growth of the first black holes, favoring light-seed formation scenarios. The same mechanism in the excited manifolds may also operate in dense, irradiated environments such as AGN outflows, linking molecular chemistry to early black hole accretion and feedback. Overall, this pathway represents a significant extension of primordial chemistry with important implications for early

structure formation and recent JWST observations of chemically enriched luminous galaxies and supermassive black holes at high redshift.

References

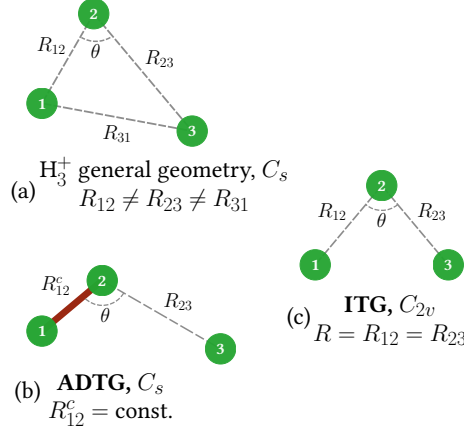
1. Barkana, R. & Loeb, A. In the beginning: the first sources of light and the reionization of the Universe. *Physics reports* **349**, 125–238 (2001).
2. Bromm, V., Yoshida, N., Hernquist, L. & McKee, C. F. The formation of the first stars and galaxies. *Nature* **459**, 49–54 (2009).
3. Bromm, V. Formation of the first stars. *Reports on Progress in Physics* **76**, 112901 (2013).
4. Tegmark, M. *et al.* How small were the first cosmological objects? *The Astrophysical Journal* **474**, 1 (1997).
5. Klessen, R. S. & Glover, S. C. The first stars: formation, properties, and impact. *Annual Review of Astronomy and Astrophysics* **61**, 65–130 (2023).
6. Greif, T. H. The numerical frontier of the high-redshift Universe. *Computational Astrophysics and Cosmology* **2**, 3 (2015).
7. Saslaw, W. C. & Zipoy, D. Molecular hydrogen in pre-galactic gas clouds. *Nature* **216**, 976–978 (1967).
8. Peebles, P. & Dicke, R. Origin of the globular star clusters. *Astrophysical Journal*, vol. 154, p. 891 **154**, 891 (1968).
9. Galli, D. & Palla, F. The dawn of chemistry. *Annual Review of Astronomy and Astrophysics* **51**, 163–206 (2013).
10. Bunker, A. J. *et al.* JADES NIRSpec Spectroscopy of GN-z11: Lyman- α emission and possible enhanced nitrogen abundance in a $z = 10.60$ luminous galaxy. *Astronomy & Astrophysics* **677**, A88 (2023).
11. Robertson, B. *et al.* Earliest galaxies in the JADES origins field: Luminosity function and cosmic star formation rate density 300 Myr after the Big Bang. *The Astrophysical Journal* **970**, 31 (2024).
12. Carniani, S. *et al.* Spectroscopic confirmation of two luminous galaxies at a redshift of 14. *Nature* **633**, 318–322 (2024).
13. Zavala, J. A. *et al.* A luminous and young galaxy at $z = 12.33$ revealed by a JWST/MIRI detection of H α and [O iii]. *Nature Astronomy* **9**, 155–164 (2025).
14. Naidu, R. P. *et al.* A cosmic miracle: A remarkably luminous galaxy at $z_{\text{spec}} = 14.44$ confirmed with JWST. *arXiv preprint arXiv:2505.11263* (2025).

15. Adamo, A. *et al.* The first billion years according to JWST. *Nature Astronomy* **9**, 1134–1147 (2025).
16. Carniani, S. *et al.* The eventful life of a luminous galaxy at $z = 14$: metal enrichment, feedback, and low gas fraction? *Astronomy & Astrophysics* **696**, A87 (2025).
17. Xiao, M. *et al.* Accelerated formation of ultra-massive galaxies in the first billion years. *Nature* **635**, 311–315 (2024).
18. Pérez-González, P. G. *et al.* The rise of the galactic empire: Ultraviolet luminosity functions at $z \sim 17$ and $z \sim 25$ estimated with the MIDIS+NGDEEP Ultra-deep JWST/NIRCam data set. *The Astrophysical Journal* **991**, 179 (2025).
19. Mason, C. A., Trenti, M. & Treu, T. The brightest galaxies at cosmic dawn. *Monthly Notices of the Royal Astronomical Society* **521**, 497–503 (2023).
20. Ferrara, A., Pallottini, A. & Dayal, P. On the stunning abundance of super-early, luminous galaxies revealed by JWST. *Monthly Notices of the Royal Astronomical Society* **522**, 3986–3991 (2023).
21. Trinca, A. *et al.* Exploring the nature of UV-bright $z \gtrsim 10$ galaxies detected by JWST: star formation, black hole accretion, or a non-universal IMF? *Monthly Notices of the Royal Astronomical Society* **529**, 3563–3581 (2024).
22. Costantin, L. *et al.* A Milky Way-like barred spiral galaxy at a redshift of 3. *Nature* **623**, 499–501 (2023).
23. Wang, W. *et al.* A giant disk galaxy two billion years after the Big Bang. *Nature Astronomy* **9**, 710–719 (2025).
24. Jain, R. & Wadadekar, Y. A grand-design spiral galaxy 1.5 billion years after the Big Bang with JWST. *Astronomy & Astrophysics* **703**, A96 (2025).
25. Fan, X., Bañados, E. & Simcoe, R. A. Quasars and the intergalactic medium at cosmic dawn. *Annual Review of Astronomy and Astrophysics* **61**, 373–426 (2023).
26. Inayoshi, K., Visbal, E. & Haiman, Z. The assembly of the first massive black holes. *Annual Review of Astronomy and Astrophysics* **58**, 27–97 (2020).
27. Volonteri, M., Habouzit, M. & Colpi, M. The origins of massive black holes. *Nature Reviews Physics* **3**, 732–743 (2021).
28. Smith, A. & Bromm, V. Supermassive black holes in the early Universe. *Contemporary Physics* (2019).
29. Jeon, J., Bromm, V., Liu, B. & Finkelstein, S. L. Physical pathways for JWST-observed supermassive black holes in the early Universe. *The Astrophysical*

Journal **979**, 127 (2025).

30. Hirata, C. M. & Padmanabhan, N. Cosmological production of H₂ before the formation of the first galaxies. *Monthly Notices of the Royal Astronomical Society* **372**, 1175–1186 (2006).
31. Grieco, F., Theulé, P., De Looze, I. & Dulieu, F. Enhanced star formation through the high-temperature formation of H₂ on carbonaceous dust grains. *Nature Astronomy* **7**, 541–545 (2023).
32. Pandey, A., Vexiau, R., Marcassa, L. G., Dulieu, O. & Bouloufa-Maafa, N. Ultracold charged atom-dimer collisions: State-selective charge exchange and three-body recombination. *Physical Review Research* **6**, 043010 (2024).
33. Yarkony, D. R. Diabolical conical intersections. *Reviews of Modern Physics* **68**, 985 (1996).
34. Coppola, C. M., Galli, D., Palla, F., Longo, S. & Chluba, J. Non-thermal photons and H₂ formation in the early Universe. *Monthly Notices of the Royal Astronomical Society* **434**, 114–122 (2013).
35. Ferretti, A., Lami, A. & Villani, G. Quantum dynamics of a model system with a conical intersection. *J. Chem. Phys.* **106**, 934–941 (1997).
36. Farfan, C. A. & Turner, D. B. A systematic model study quantifying how conical intersection topography modulates photochemical reactions. *Phys. Chem. Chem. Phys.* **22**, 20265–20283 (2020).
37. Juodžbalis, I. *et al.* JADES—the Rosetta stone of JWST-discovered AGN: deciphering the intriguing nature of early AGN. *Monthly Notices of the Royal Astronomical Society* **535**, 853–873 (2024).
38. Maiolino, R. *et al.* JADES-The diverse population of infant black holes at $4 < z < 11$: Merging, tiny, poor, but mighty. *Astronomy & Astrophysics* **691**, A145 (2024).
39. Matthee, J. *et al.* Little red dots: an abundant population of faint active galactic nuclei at $z \sim 5$ revealed by the EIGER and FRESCO JWST surveys. *The Astrophysical Journal* **963**, 129 (2024).
40. Taylor, A. J. *et al.* CAPERS-LRD-z9: A gas-enshrouded Little Red Dot hosting a broad-line Active Galactic Nucleus at $z = 9.288$. *The Astrophysical Journal Letters* **989**, L7 (2025).
41. Harrison, C. M. & Ramos Almeida, C. Observational tests of active galactic nuclei feedback: An overview of approaches and interpretation. *Galaxies* **12**, 17 (2024).
42. Alexander, D. *et al.* What drives the growth of black holes: A decade of progress. *New Astronomy Reviews* 101733 (2025).

43. Riffel, R. A., Zakamska, N. L. & Riffel, R. Active galactic nuclei winds as the origin of the H₂ emission excess in nearby galaxies. *Monthly Notices of the Royal Astronomical Society* **491**, 1518–1529 (2020).
44. Gallagher, R. *et al.* Widespread star formation inside galactic outflows. *Monthly Notices of the Royal Astronomical Society* **485**, 3409–3429 (2019).
45. Richings, A. J. & Faucher-Giguere, C.-A. The origin of fast molecular outflows in quasars: molecule formation in AGN-driven galactic winds. *Monthly Notices of the Royal Astronomical Society* **474**, 3673–3699 (2018).
46. Ripamonti, E. The role of HD cooling in primordial star formation. *Monthly Notices of the Royal Astronomical Society* **376**, 709–718 (2007).
47. Mebane, R. H., Mirocha, J. & Furlanetto, S. R. The persistence of Population III star formation. *Monthly Notices of the Royal Astronomical Society* **479**, 4544–4559 (2018).
48. Madau, P. & Rees, M. J. Massive black holes as population III remnants. *The Astrophysical Journal* **551**, L27 (2001).
49. Lupi, A., Quadri, G., Volonteri, M., Colpi, M. & Regan, J. A. Sustained super-Eddington accretion in high-redshift quasars. *Astronomy & Astrophysics* **686**, A256 (2024).
50. Johnson, J. L. & Bromm, V. The aftermath of the first stars: massive black holes. *Monthly Notices of the Royal Astronomical Society* **374**, 1557–1568 (2007).
51. O’Brennan, H. *et al.* Predicting the number density of heavy seed massive black holes due to an intense Lyman-Werner field. *arXiv preprint arXiv:2502.00574* (2025).
52. Suh, H. *et al.* A super-Eddington-accreting black hole ~ 1.5 Gyr after the Big Bang observed with JWST. *Nature Astronomy* **9**, 271–279 (2025).
53. Ighina, L. *et al.* X-Ray investigation of possible super-Eddington accretion in a radio-loud quasar at $z = 6.13$. *The Astrophysical Journal Letters* **990**, L56 (2025).
54. Geris, S. *et al.* JADES reveals a large population of low-mass black holes at high redshift. *Monthly Notices of the Royal Astronomical Society* **545**, staf1979 (2026).
55. Maiolino, R. *et al.* A small and vigorous black hole in the early Universe. *Nature* **627**, 59–63 (2024).
56. Reines, A. E. & Volonteri, M. Relations between central black hole mass and total galaxy stellar mass in the local Universe. *The Astrophysical Journal* **813**, 82 (2015).



Extended Data Fig. 1 | H_3^+ geometries. (a) Three H^+ cores labeled as 1, 2, 3, and the set of internal coordinates R_{12} , R_{23} , θ ($\angle 123$). (b) The atom-dimer triangle geometry (ADTG), belonging to the C_s point group, with R_{12} fixed to a given value R_{12}^c . (c) The isosceles triangle geometry (ITG) belonging to the C_{2v} point group, with $R_{12} = R_{23} \equiv R$ for a given θ .

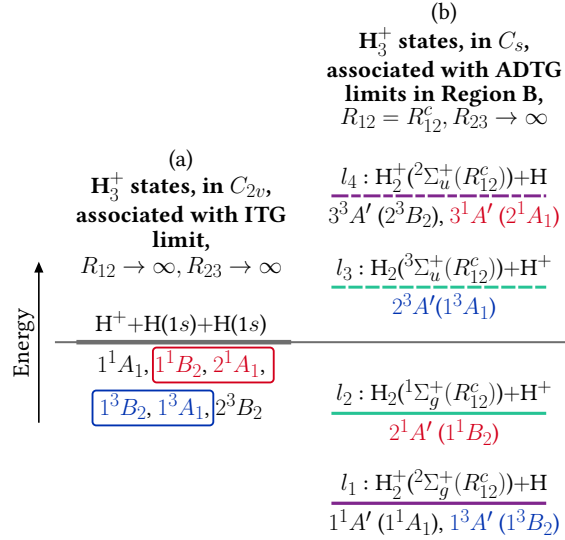
5 Methods

5.1 Acronyms and conventions

In the manuscript, whenever it is not stated explicitly, labels $^1\Sigma_g^+$ and $^3\Sigma_u^+$ are used for the ground and first excited electronic states of H_2 , i.e., $X^1\Sigma_g^+$ and $a^3\Sigma_u^+$ for brevity, respectively. These states are associated with $\text{H}(1s)+\text{H}(1s)$ in the asymptotic limit. Similarly, $^2\Sigma_g^+$ and $^2\Sigma_u^+$ are used for the ground and first excited H_2^+ states, i.e., $X^2\Sigma_g^+$ and $A^2\Sigma_u^+$, respectively, both associated with $\text{H}^++\text{H}(1s)$ limit. $\text{H}_2(g/u)$ and $\text{H}_2^+(g/u)$ also represent these states. H and H^- stand for $\text{H}(1s)$ and $\text{H}^-(1s^2)$, respectively. A similar convention is used for deuterium (D) as well. The main acronyms used in the discussion of JT-induced TTBR+CE mechanism are listed in Extended Data Table 1.

TTBR	Transient Three-Body Recombination
CE	Charge Exchange
JT coupling	Jahn-Teller coupling
ETG	Equilateral Triangle Geometry
ITG	Isosceles Triangle Geometry
ADTG	Atom-Dimer Triangle Geometry
MEC	Minimal Energy Configuration
PES	Potential Energy Surface

Extended Data Table 1 | **List of acronyms.** Main acronyms used in the discussion of JT-induced TTBR+CE mechanism for H_2 formation.

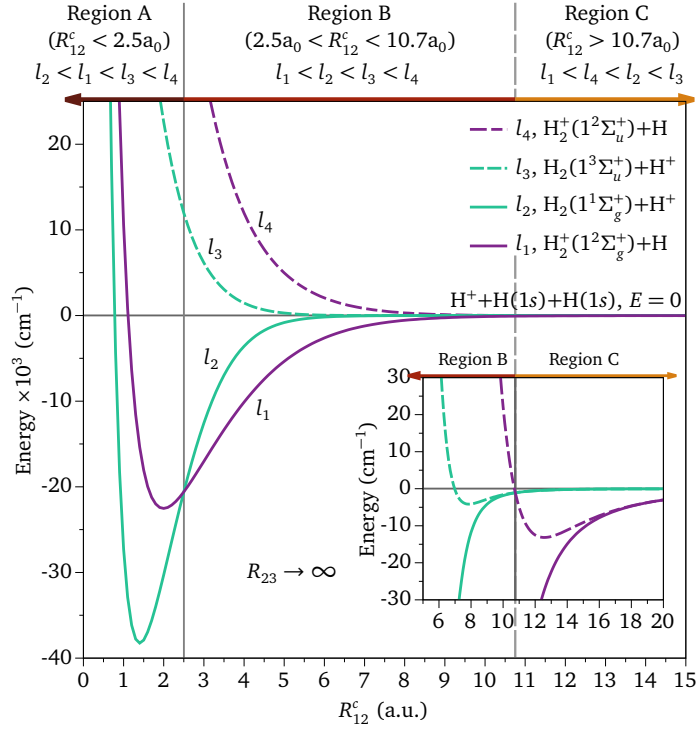


Extended Data Fig. 2 | H₃⁺ asymptotic limits and states. (a) For H⁺, H(1s), H(1s) system in ITG, six H₃⁺ states are represented in C_{2v} point group and have a common asymptotic limit at $E = 0 \text{ cm}^{-1}$, representing $R_{12} = R_{23} \rightarrow \infty$. (b) six H₃⁺ states in C_s point group, associated with four ADTG asymptotes H₂(g/u)+H⁺ (i.e. l_2 and l_3 , resp.) and H₂⁺(g/u)+H(1s) (i.e. l_1 and l_4 , resp.) for a given dimer size belonging in Region B, ($2.5a_0 < R_{12}^c < 10.7a_0$, and $l_1 < l_2 < l_3 < l_4$), with $R_{23} \rightarrow \infty$.

5.2 JT-induced TTBR+CE reactions on the singlet H₃⁺ states

To describe the nuclear dynamics of H⁺, H(1s), and H(1s) system, potential energy surfaces (PESs) of H₃⁺ is expressed as a function of internal coordinates for three H⁺ nuclei, namely R_{12} , R_{23} , and $\theta(\angle 123)$, see Extended Data Fig. 1(a). Two special molecular geometries and the respective one-dimensional cuts to the PESs (PECs) are used to address TTBR and CE of Eq. 1. The first geometry, Atom-Dimer Triangle Geometry (ADTG), keeps the internuclear distance R_{12} fixed at R_{12}^c for a given θ , thereby modeling a non-dissociating dimer within the H₃⁺ complex, as shown in Extended Data Fig. 1(b). This setup adequately describes the CE reactions occurring between the charged atom-dimer complex. The second geometry, Isosceles Triangle Geometry (ITG), sets $R_{12} = R_{23} \equiv R$ for a chosen θ , as depicted in Extended Data Fig. 1(c). This arrangement is suitable for analyzing TTBR in the collision of H⁺ with two H(1s) atoms. H₃⁺ electronic states in ADTG are represented in the low-symmetry C_s point group, exhibiting only a planar symmetry. Whereas H₃⁺ states in ITG are represented in C_{2v} point group, which has a two-fold rotation axis and two vertical mirror planes. When $\theta = 60^\circ$, ITG becomes Equilateral Triangle Geometry (ETG), exhibiting additional symmetry elements of D_{3h} point group, which trace the seams of the JT-coupled states.

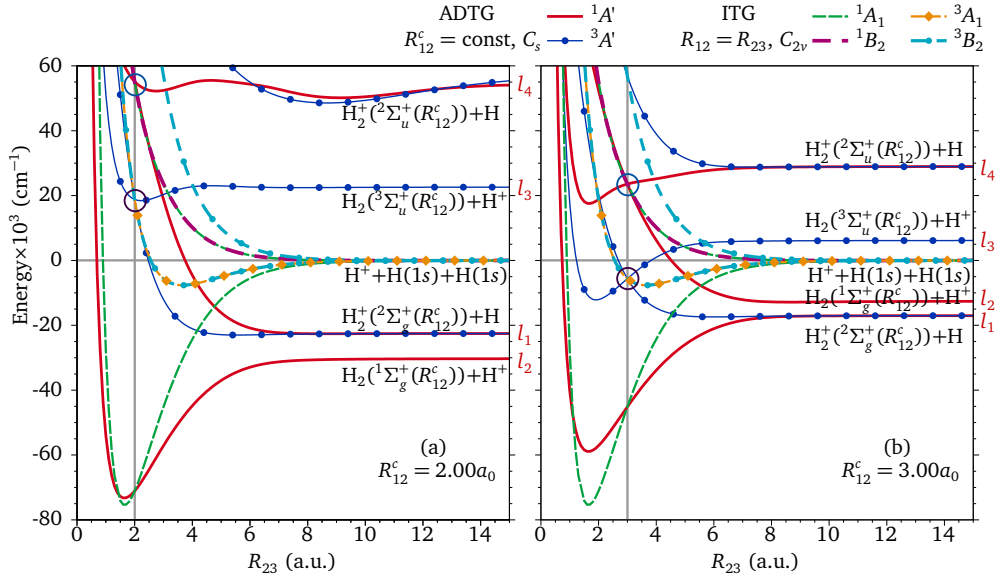
For H⁺+H(1s)+H(1s) complex, six states of H₃⁺ (three singlets and three triplets) in ITG and ADTG are shown in Extended Data Fig. 2(a) and (b), respectively, along with their asymptotic limits. For ITG (represented in C_{2v} point group), singlet and



Extended Data Fig. 3 | ADTG asymptotic limits. Energies of l_1 , l_2 , l_3 , and l_4 , as a function of the dimer size, R_{12}^c , with atom-dimer distance, $R_{23} \rightarrow \infty$. Three Regions, A, B, and C, are identified based on the energy ordering of the ADTG asymptotic limits. The inset shows the onset of Region C where both ADTG asymptotes associated with ionic dimers, $H_2^+(g/u)$, (i.e., l_1 and l_4), become lower than the ones associated with neutral ones, $H_2(g/u)$, (i.e., l_2 and l_3).

triplet H_3^+ states are 1^1A_1 , 1^1B_2 (associated with $S1$ of Fig. 1), 2^1A_1 (associated with $S2$ of Fig. 1), and 1^3B_2 , 1^3A_1 , 2^3B_2 , respectively (see Extended Data Fig. 2(a)). The singlet and triplet JT-coupled pairs are marked by rectangles. In contrast, for ADTG, which is represented in the C_s point group, both singlet and triplet H_3^+ states are labeled as A' (see Extended Data Fig. 2(b)). The associated ITG states are also shown in round brackets. H_3^+ states in ITG have a common asymptotic limit with $R_{12} = R_{23} \rightarrow \infty$, representing the fully atomized ion-atom-atom limit, $E = 0 \text{ cm}^{-1}$, shown by a horizontal line in Extended Data Fig. 2(a). On the other hand, there are four ADTG asymptotic limits, i.e., $H_2^+(g/u)+H$ (l_1 and l_4) and $H_2(g/u)+H^+$ (l_2 and l_3), as shown in Extended Data Fig. 2(b). It is important to notice that a singlet and a triplet H_3^+ states are associated with both ADTG limits with ionic dimers, i.e., l_1 and l_4 . For ADTG limits with neutral dimers, l_2 and l_3 , only one state (either singlet or triplet) is connected to each limit.

Energies of the four ADTG asymptotic limits, l_1 , l_2 , l_3 , and l_4 , as a function of the dimer size, R_{12}^c , for $R_{23} \rightarrow \infty$, are shown in Extended Data Fig. 3. Region A ($R_{12}^c < 2.5a_0$, with $l_2 < l_1 < l_3 < l_4$), Region B ($2.5a_0 < R_{12}^c < 10.7a_0$, with

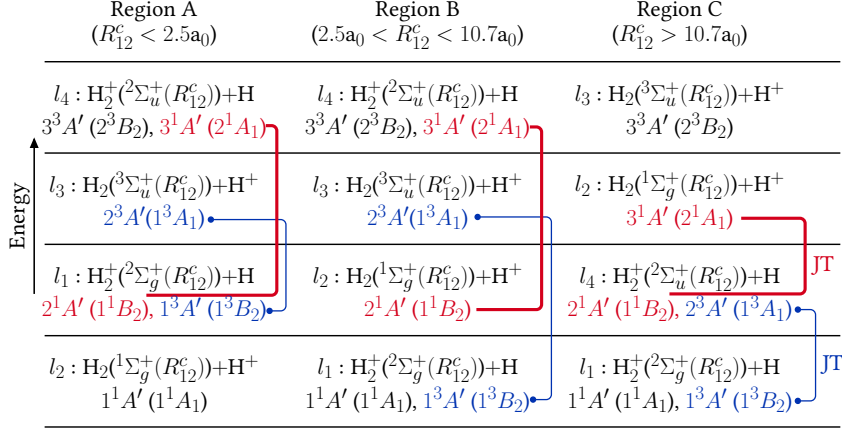


Extended Data Fig. 4 | H_3^+ states in ADTG and ITG. Three singlet and three triplet states of H_3^+ in ADTG and ITG for $\theta = 60^\circ$ associated with the first fully atomized limit, $\text{H}^+ + \text{H}(1s) + \text{H}(1s)$. ADTG states are presented for $R_{12}^c = 2.00a_0$ (corresponds to Region A, Extended Data Fig. 3), and for $R_{12}^c = 3.00a_0$ (Region B, Extended Data Fig. 3), in Extended Data Fig. 4 (a) and (b), respectively. The energy ordering change of the ADTG asymptotes (l_1, l_2, l_3, l_4) is also indicated. ITG H_3^+ states, which are identical in both panels, all dissociate to $\text{H}^+ + \text{H}(1s) + \text{H}(1s)$. Vertical lines at $R_{23} = 2.00a_0$ in Extended Data Fig. 4(a) and $R_{23} = 3.00a_0$ in Extended Data Fig. 4(b) mark the geometries where the JT-coupling condition is met, i.e., $R_{23} = R_{12}^c, \theta = 60^\circ$ (the ETG). Circles highlight observed JT couplings in the second and third singlet, $2^1A'$ & $3^1A'$; S1 and S2 of Fig. 1, and first and second triplet, $1^3A'$ & $2^3A'$, H_3^+ states. The corresponding singlet ITG states, $1^1B_2, 2^1A_1$, that are degenerate at $\theta = 60^\circ$, represent the seam of the JT-coupling in S1 and S2, shown in Fig. 1(d). For the triplet JT-coupled pairs, these are $1^3B_2, 1^3A_1$ states.

$l_1 < l_2 < l_3 < l_4$), and Region C ($R_{12}^c > 10.7a_0$, with $l_1 < l_4 < l_2 < l_3$) mark the domains in which the energy ordering of the four ADTG limits are different.

H_3^+ PESs are computed under the Born-Oppenheimer approximation using the MOLPRO package⁵⁷. The complete active-space self-consistent field (CASSCF) and multireference configuration interaction (MRCI-SD) methods, which include single and double electronic excitations, are utilized⁵⁸. Calculations use an augmented correlation-consistent basis set, av5z, for hydrogen atoms and are benchmarked against previous studies^{59,60}.

In Extended Data Fig. 4 (a) and (b), ADTG and ITG states of H_3^+ are shown for $\theta = 60^\circ$, in the internuclear separation space, where both R_{12} and R_{23} are finite. For the ADTG states, R_{12}^c is $2.00a_0$ in Extended Data Fig. 4(a), representative of Region A. In Extended Data Fig. 4(b), R_{12}^c is $3.00a_0$, representative of Region B. The energy orderings of the ADTG asymptotes are provided in both panels; as we can see, they are consistent with Extended Data Fig. 3. Vertical lines at $R_{23} = 2.00a_0$ in Extended Data Fig. 4(a) and $R_{23} = 3.00a_0$ in Extended Data Fig. 4(b) mark the evolution of ADTG

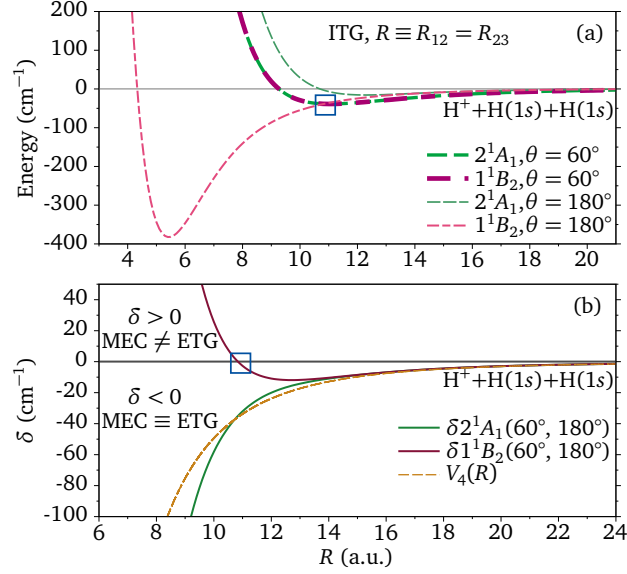


Extended Data Fig. 5 | Energy ordering of ADTG limits. Energy ordering of l_1, l_2, l_3, l_4 , in Regions A, B, and C. The JT-coupled ADTG singlet ($2^1A'(S1)$ & $3^1A'(S2)$) and triplet ($1^3A'$ & $2^3A'$) H_3^+ electronic states, linked by the right brackets, are associated with different ADTG limits in Regions A, B, and C. The possibility of CE in the JT-coupled singlet states, $S1$ and $S2$, involving the transition state $\{\text{H}_2^+(\text{}^2\Sigma_u^+)+\text{H}(1s)\}$ of Eq. 1, is decided by whether the outgoing JT-coupled state leads to $\text{H}_2(g)$ dimer in the ADTG limit (as depicted in Fig. 1(e)).

states to the ETG, where the condition for the JT-coupling is met, i.e., $R_{23} = R_{12}^c$, $\theta = 60^\circ$. At these points, marked by circles above the vertical lines, the second and third singlet states ($2^1A', 3^1A'$; $S1$ and $S2$ from Fig. 1) and the first and second triplet states ($1^3A', 2^3A'$) become degenerate. The corresponding ITG singlet ($1^1B_2, 2^1A_1$; associated with $S1$ and $S2$ of Fig. 1(d)) and triplet ($1^3B_2, 1^3A_1$) states are degenerate for all internuclear separations at ETG and represent the seams of JT coupling in H_3^+ . For $\theta \neq 60^\circ$, ADTGs represent isosceles triangles at $R_{23} = R_{12}^c$, which lifts the degeneracy between JT-coupled states. The influence of geometry on JT-induced TBR and CE collisions in a similar system, Rb_3^+ , has been discussed previously⁶¹.

The CE channel in Eq. 1 can proceed via JT-induced coupling between the singlet H_3^+ states, $S1$ and $S2$. Whether the JT coupling permits CE reactions is determined by the energy ordering of the ADTG asymptotes in Regions A, B, and C, as shown in Extended Data Fig. 5. Specifically, the constraint arises because the JT coupling consistently links the second and third singlet states, $2^1A'(S1)$ and $3^1A'(S2)$, across all internuclear separations. For Eq. 1, the transition state $\{\text{H}_2^+(\text{}^2\Sigma_u^+)+\text{H}(1s)\}$ is associated with $2^1A'(S1)$ in Region C and with $3^1A'(S2)$ in Region B. In both Regions B and C, this atom-dimer transition complex then connects, via Jahn-Teller coupling, to $\text{H}_2(\text{}^1\Sigma_g^+)+\text{H}^+$, enabling charge exchange. In contrast, in Region A, as shown in Extended Data Fig. 5, the JT-coupled singlet state $3^1A'$, associated with $\{\text{H}_2^+(\text{}^2\Sigma_u^+)+\text{H}(1s)\}$, does not support charge exchange, but only electronic symmetry exchange in H_2^+ , i.e., $u \leftrightarrow g$.

Another important constraint in the TTBR and CE reactions is that JT-coupling occurs only at equilateral triangles, as shown in Fig. 1(d). For a collision between H^+ , $\text{H}(1s)$, and $\text{H}(1s)$ that begins in a random orientation in hydrogen gas, the equilateral triangle must be the MEC. If so, geometry rearrangement during the collision can then drive the system toward the ETGs. To describe the geometry rearrangement



Extended Data Fig. 6 | Minimal energy configuration determination. (a) One-dimensional cuts of the PESs of H_3^+ ITG states 1^1B_2 , 2^1A_1 (associated with ADTG $2^1A'(S1)$ & $3^1A'(S2)$ states, respectively) involved in the JT coupling, for $R_{12} = R_{23} \equiv R < 21a_0$, and for $\theta = 60^\circ$ and 180° . Both curves are degenerate for 60° (the ETG, identical to one depicted in Fig. 1(d)) with the well depth of -38.7 cm^{-1} at $R = 11.10a_0$. Panel (b) shows the energy difference, δ , between the PECs at $\theta = 60^\circ$ and 180° , highlighting that for the 1^1B_2 curve, the latter geometry has a minimal energy for $R < 10.9a_0$ (squared box). For the large R , δ for both states show $V_4(R)$ nature, where $V_4(R) = -C_4/R^4$, with $2C_4 = \alpha_d = 4.5 \text{ a.u.}$ 2^1A_1 shows its minima for 60° geometry for all molecular sizes.

on the JT-coupled singlet states of H_3^+ , their ITG states, 1^1B_2 and 2^1A_1 (associated with $S1$ and $S2$, respectively), are shown for $\theta = 60^\circ$ and $\theta = 180^\circ$ in Extended Data Fig. 6 (a). Energies of all other geometries for $60^\circ < \theta < 180^\circ$ fall in between these two extremes. As discussed earlier, 1^1B_2 and 2^1A_1 ITG curves are degenerate for $\theta = 60^\circ$ at all internuclear separations, representing the seam of the JT-coupled states (also shown in Extended Data Fig. 4 (a) and (b)). The energy differences between these two geometries for the states, $\delta 1^1B_2(60^\circ, 180^\circ)$ and $\delta 2^1A_1(60^\circ, 180^\circ)$, are shown in Extended Data Fig. 6 (b). A negative δ represents the minima for $\theta = 60^\circ$, i.e., the region where MEC is identical to the ETG, enabling the occurrence of JT-coupling. When $\delta > 0$, linear geometry ($\theta = 180^\circ$) becomes the MEC, thereby prohibiting the JT-coupling. In Region B, the transition complex $\{\text{H}_2^+(^2\Sigma_u^+) + \text{H}(1s)\}$ of Eq. 1 is associated with the 2^1A_1 ITG state (see Extended Data Fig. 5). This state exhibits minima for $\theta = 60^\circ$ for all interparticle separations, i.e., $\delta < 0 \forall R$. Thus, ensuring the occurrence of Jahn-Teller coupling between H_3^+ singlet states. In Region C, on the other hand, $\{\text{H}_2^+(^2\Sigma_u^+) + \text{H}(1s)\}$ is associated with the 1^1B_2 ITG state. This state shows minima for the ETG for $R(\equiv R_{12} = R_{23}) > 10.9a_0$, i.e., $\delta < 0 \forall R > 10.9a_0$, marked by a square in Extended Data Fig. 6 (a) and (b). It covers almost the entire Region C, defined in the ADTG asymptotic limit as $R_{12}^c > 10.7a_0$ with $R_{23} \rightarrow \infty$. Therefore, in Region C, as well, TTBR and CE would occur. These possibilities are summarized in Extended Data Table 2.

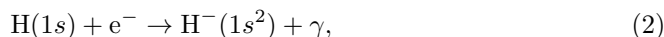
ADTG states of $\{H_2^+(^2\Sigma_u^+(R_{12}^c))+H\}$ in the asymptotic limit; $R_{23} \rightarrow \infty$	JT-coupled outgoing channels and H_3^+ states	CE
Region A, $R_{12}^c < 2.5a_0$, $3^1A'(60^\circ \forall R)$	$H_2^+(X^2\Sigma_g^+)+H$, $2^1A'$	No
Region B, $2.5a_0 < R_{12}^c < 10.7a_0$, $3^1A'(60^\circ \forall R)$	$H_2(X^1\Sigma_g^+)+H^+$, $2^1A'$	Yes
Region C, $R_{12}^c > 10.7a_0$, $2^1A'(60^\circ \forall R > 10.9a_0)$	$H_2(X^1\Sigma_g^+)+H^+$, $3^1A'$	Yes

Extended Data Table 2 | Charge exchange prospects. The possibilities of charge exchange between $H_2^+(^2\Sigma_u^+(R_{12}^c))$ and H, i.e., the transition state of Eq. 1, in the ADTG asymptotic limit in Regions A, B, and C are summarized, combining the information from Extended Data Fig. 3, 5, and 6. The initial ADTG electronic state with the position in θ of its minimal energy configuration for ITG is also provided in the first column, recalling that CE will be possible via JT coupling only for $\theta = 60^\circ$. In the second column, ADTG asymptotes and the associated states of the outgoing channels are provided. In Regions B and C, CE is allowed via JT coupling. However, in Region A, JT-induced reaction would only allow exchange of H_2^+ molecular ion symmetry from u to g .

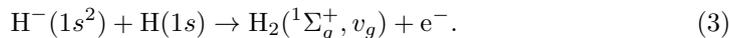
It is important to note that, in the current manuscript, we left out two reaction channels. The first involves reactions on the triplet JT-coupled states of H_3^+ . Collisions on the JT-coupled triplet states would produce $H_2^+(^2\Sigma_g^+)$ in a TBR reaction. However, the subsequent CE channel would connect them to the ungerade states of either H_2 or H_2^+ , which are either weakly bound or unstable (see Extended Data Fig. 5). Eq. 1 also leaves out the TBR collisions that directly create neutral H_2 . This is because the TBR rate for producing weakly bound neutral dimers would be much lower—about 2 to 4 orders of magnitude—than that for producing weakly bound molecular ions, as discussed for many ion-atom-atom cases^{62,63}.

5.3 Comparison of H^- and H_2^+ mechanisms with JT-induced TTBR+CE mechanism at high-redshifts

The standard pathways of H_2 formation involving H^- and H_2^+ intermediates, and their role in the creation of first stars in the early Universe were identified as early as the 1960s^{64,65}. Saslaw & Zipoy first calculated H_2 abundance based on the H_2^+ mechanism in the primordial Universe⁶⁴. H_2 production by the H^- mechanism was first suggested by Peebles & Dicke⁶⁵. In the H^- mechanism, H_2 formation occurs by a two-step reaction pathway involving the H^- ion created by radiative attachment as an intermediate step^{65,66},



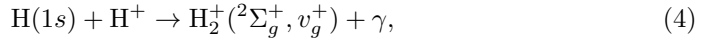
followed by production of H_2 by associative detachment,



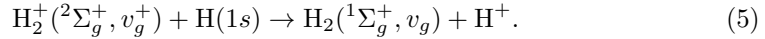
$H_2(^1\Sigma_g^+, v_g)$ produced by Eq. 3 are predominantly created in its excited vibrational levels $v_g = 4 - 7$ ⁶⁷. As discussed earlier, the H^- mechanism is the dominant reaction channel for H_2 formation at redshift $z \simeq 30 - 20$ when the first stars formed⁶⁸. Second pathway of H_2 formation, referred as H_2^+ mechanism, involves production of H_2^+ by radiative association⁶⁴,

	H ⁻ mechanism	H ₂ ⁺ mechanism	JT-induced TTBR+CE mechanism
Production processes	Two-step Intermediate: H ⁻	Two-step Intermediate: H ₂ ⁺	One-step No intermediate
Suppression processes	Inverse of the 1st-step. CMBR.	Inverse of the 1st-step. CMBR.	Not affected by CMBR
Primary source	at $z < 100$	at $100 < z < 300$	at $z \leq 1100$, AGN outflows
main HD production	Secondary bond-rearrangement	Secondary bond-rearrangement	Direct
Exited state channels	No excited state	Strongly suppressed (if present)	Multiple pathways in H ₃ ^{+*} , possibly active in AGNs
Formation of the first stars and black holes	at $20 < z < 30$ Pop III.1 pathway simulation		at $30 < z < 50$ (see text) HD-dominated cooling

Extended Data Table 3 | Main H₂ formation pathways. A comparison of the standard H⁻ and H₂⁺ mechanisms for H₂ formation with the proposed JT-induced TTBR+CE mechanism. The major advantage of JT-induced TTBR+CE mechanism, being a single-step reaction, is its immunity against photodissociation by CMB radiation, which strongly suppresses the H⁻ and H₂⁺ intermediates and limits H₂ production in the early Universe ($z > 100$) (see text for details). Given this, H₂ and HD could be produced from the JT-induced TTBR+CE mechanism much earlier, right towards the end of the epoch of recombination ($z \leq 1100$), which may facilitate the efficient molecular cooling. In the Pop III.2 scenario, HD-dominated cooling occurs only at later stages, when HD production rises from the bond-rearrangement reaction, a secondary process dependent on high abundances of H₂ and D⁺, and therefore requiring additional favorable conditions. In contrast, HD formation via the JT-induced TTBR+CE mechanism could enable early star formation in HD-cooled primordial gas. Depending on the reaction rate, the first stars and black holes might appear significantly earlier. Additionally, JT-coupled reactions producing H₂ and HD in the excited states of H₃^{+*} could provide previously overlooked cooling channels in AGNs and their outflows, enhancing star formation and black hole growth, and driving BH-galaxy coevolution.



followed by the charge transfer reaction,



Radiative association of H(1s) and H⁺ creates H₂⁺(²Σ_g⁺, v_g⁺) mostly in its excited vibrational levels $v_g^+ > 10$ ⁶⁹. The charge exchange reaction $\text{H}_2^+ (^2\Sigma_g^+, v_g^+, j^+) + \text{H} \rightarrow \text{H}_2 (^1\Sigma_g^+, v_g, j) + \text{H}^+$ has been studied extensively. These studies focus on calculating cross-sections and exploring vibrational level dependence^{60,70–76}. It is important to note that in charge exchange reactions, such as the one given in Eq. 5, and in the three-body, diatomic association like $\text{H}^+ + \text{H}(1s) + \text{H}(1s)$, studied by Krstic *et al.*⁷⁷, H₂⁺ and H₂ are both considered in their ground states, i.e., H₂⁺(X²Σ_g⁺) and H₂(X¹Σ_g⁺). Their charge-exchange interactions with H(1s) or H⁺ are therefore described by couplings between the first and second singlet states of the H₃⁺ complex, rather than by the Jahn-Teller-coupled second and third singlet states^{60,70–77}.

The initial steps of both the H⁻ and H₂⁺ formation mechanisms (Eq. 2 and Eq. 4, respectively) are intrinsically slow⁷⁸. Nevertheless, the H⁻ pathway is generally more

efficient under typical conditions, as its formation rate is roughly an order of magnitude higher than that of H_2^+ ^{69,78}. At high redshift, however, the CMB strongly suppresses this channel. $\text{H}^-(1s^2)$ is only weakly bound (~ -0.75 eV ⁷⁹, whereas $\text{H}_2^+(^2\Sigma_g^+, v_g^+ = 0)$ is more strongly bound (~ -2.65 eV ⁸⁰), making photodetachment particularly effective for H^- . Consequently, for $z > 100$ the H^- route contributes very little to H_2 production, and the H_2^+ pathway becomes the dominant formation channel ^{69,81}.

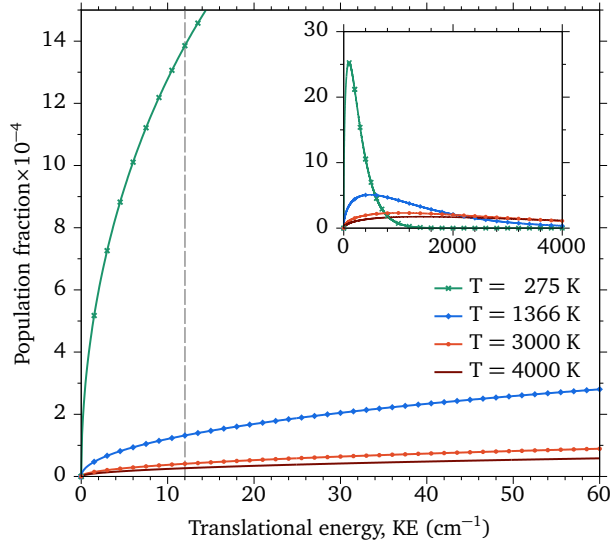
Even so, H_2^+ formed by radiative association is mainly created in highly excited vibrational levels of the $X^2\Sigma_g^+(v_g^+)$ state. Decay to lower vibrational levels is slow, occurring only via weak quadrupole transitions. In contrast, as photodissociation back to the $A^2\Sigma_u^+(v_u^+)$ continuum is a dipole-allowed transition, most newly formed H_2^+ is destroyed before it reacts to form H_2 . This vibrational sensitivity also makes the H_2^+ channel inefficient at early times, further lowering the primordial H_2 abundance ^{68,69}. Aspects of H_2 formation from the H^- and H_2^+ mechanisms, along with the proposed JT-induced TTBR+CE mechanism, are summarized in Extended Data Table 3.

5.4 Energy constraint for JT-induced reactions at the high-redshift thermodynamic conditions

We previously found that JT coupling between the $S1$ and $S2$ states of H_3^+ occurs only at ETGs. On the other hand, three-body collisions involving H^+ and two $\text{H}(1s)$ atoms begin from random geometries, with their evolution determined by the interplay between the total initial kinetic energies (KEs) of the particles and the system’s interaction potential, which drives it toward the minimum energy configuration (MEC). The initial KEs of H^+ and the $\text{H}(1s)$ atoms are depicted in Fig. 1(a). It is important to note that the nuclei’s KEs are not included in the calculation of the potential energy surfaces (PESs) under the fixed-nuclei Born-Oppenheimer approximation. Instead, nuclear KEs influence the collision dynamics, with the computed PES serving as the guiding potential for their motion.

The well depth of H_3^+ singlet states, $S1$ and $S2$ (1^1B_2 and 2^1A_1 , respectively, in ITG; both are degenerate at ETGs), is -38.7 cm^{-1} for an equilateral triangle of sides equal to $11.10a_0$. See Extended Data Fig. 6 (a). In addition to the condition for JT-induced reactions shown in Fig. 1(d), the finite well depth of the PESs adds further restrictions on the reaction. Specifically, the sum of the initial KEs of the ion-atom-atom triad must be less than the well depths of $S1$ and $S2$ for the participants to be effectively guided by these PESs. To assess the effect of this restriction, we consider a simplified picture. In this model, each colliding partner—the H^+ ion or each of the two H atoms—should have KE below 12.9 cm^{-1} (meaning 3×12.9 $\text{cm}^{-1} < 38.7$ cm^{-1}) for geometry rearrangement to occur during collisions. In the present analysis, we have assumed a rather stronger condition on particles’ energies, $\text{KE} < 12$ cm^{-1} .

If the well depths of the PESs imposed no energy constraints, the entire H gas ensemble at temperature T would be available for such a reaction. However, because the present case requires particle KE to be < 12 cm^{-1} , at any given moment only a fraction, P_k , of the thermal gas has H atoms with $\text{KE} < 12$ cm^{-1} . For $T = 275$ K, 1366 K, 3000 K, and 4000 K, $P_k(\text{KE} < 12$ $\text{cm}^{-1})$ are 0.011363, 0.001059, 0.000327, and 0.000213, respectively, as shown in Extended Data Fig. 7. Meanwhile, due to ongoing collisions among H atoms, the subset of atoms satisfying the $\text{KE} < 12$ cm^{-1} constraint



Extended Data Fig. 7 | Energy constrained population fraction. Maxwell-Boltzmann probability distributions for $T = 275$ K, 1366 K, 3000 K, and 4000 K, representing the CMB temperatures at $z = 100, 500, 1100,$ and $1500,$ respectively. The vertical line at 12 cm^{-1} marks the kinetic energy limit, ($\text{KE} < 12 \text{ cm}^{-1}$), for H or H^+ in the ion-atom-atom collision, relevant to Jahn-Teller reactions on singlet H_3^+ PESs, $2^1A'(S1)$ and $3^1A'(S2)$, needed for geometry rearrangement. The inset shows the probability distributions over a wider energy range.

is constantly changing. As a result, over time, every H atom in the gas can meet the energy constraint at some point. These collisions also ensure that whenever low-energy H atoms are removed through TTBR and CE reactions, other H atoms adjust to satisfy the $\text{KE} < 12 \text{ cm}^{-1}$ constraint. This process maintains the Maxwell-Boltzmann distribution, preserving P_k as a statistical invariant.

For the JT-induced reaction to remain unaffected by the energy constraint, the timescale in which the entire gas ensemble satisfies the energy constraint must be much shorter than the reaction timescales. The time required for the full hydrogen gas ensemble to reach a state in which the kinetic energy of each H atom satisfies $\text{KE} < 12 \text{ cm}^{-1}$ at least once is $t_R = (1/P_k) \star t_f$. Where the mean-free time, t_f , for hard-sphere elastic collisions that change the speed of H atoms is $t_f = 1/(\sigma \times \langle v \rangle \times n_H)$; $\sigma = \pi(2r)^2$ is the collision cross section with H atoms of radius $r = 2.5 a_0$, $\langle v \rangle$ is the mean speed of H atoms at temperature T, and n_H is the hydrogen gas density. For $T = 3000$ K (representative of CMB temp. at $z = 1100$ with $n_H \sim 2.1 \times 10^3 \text{ cm}^{-3}$) and $T = 4000$ K ($z = 1500$ with $n_H \sim 5.4 \times 10^3 \text{ cm}^{-3}$), t_R are 74.42 and 45.15 years, respectively. Varying the hard-sphere size in the range of $r = 2.0a_0$ to $4.0a_0$ that covers the strong interaction domain for $\text{H}_2X^1\Sigma_g^+$ state would change the t_R by factors of 1.56 to 0.40. In short, at high redshifts near the epoch of recombination, t_R would be a few tens of years.

Using the probability P_k at temperature T, we also estimate the time, t_N , for three-body collisions where each participant must have KE less than 12 cm^{-1} . In t_N

time, every site in the H gas ensemble at density n_{H} becomes eligible for reaction. At $T = 3000$ K and $T = 4000$ K, t_N is 0.38 years and 1.78 years, respectively.

Considering the larger time scale from t_R and t_N , and for the H density ($n_{\text{H}}, n_{\text{H}^+}$ are $\sim 10^3 \text{ cm}^{-3}$) of the early Universe at $z = 1100, 1500$, collision rates for the hard-sphere, t_R , with the energy constraint, $\text{KE} < 12 \text{ cm}^{-1}$, would be $\sim 10^{-5} \text{ cm}^{-3} \text{ s}^{-1}$.

For comparison, the total recombination rate for three-body collisions between an H^+ ion and two H atoms is $\sim 10^{-22} \text{ cm}^{-3} \text{ s}^{-1}$. Here, K_3 is $\approx 10^{-31} \text{ cm}^6 \text{ s}^{-1}$ at $T \sim 1000$ K⁶². With non-adiabatic corrections, it could reach $\sim 10^{-18} \text{ cm}^{-3} \text{ s}^{-1}$. It is, therefore, 17 (the usual) to 13 (with non-BO corrections for the JT-induced TTBR+CE reactions) orders of magnitude smaller than the rate for hard-sphere collisions at typical conditions.

For temperature $T \sim 1000$ K corresponding to $z \approx 1000$, and densities of H, H^+ , and $e^- \sim 10^3 \text{ cm}^{-3}$, collision rates of other reactions of interest for H_2 formation in the early Universe, too, are many orders of magnitude smaller than the hard-sphere collision rates. For example, the first step of the H_2^+ mechanism (Eq. 2) has collision rate $\sim 10^{-11} \text{ cm}^{-3} \text{ s}^{-1}$, (considering the rate coefficient of H_2^+ radiative association $\sim 10^{-17} \text{ cm}^3 \text{ s}^{-1}$ ⁷⁸). The first step of the H^- mechanism (Eq. 4), it is $\sim 10^{-9} \text{ cm}^{-3} \text{ s}^{-1}$, (with rate coefficient of H^- radiative attachment $\sim 10^{-15} \text{ cm}^3 \text{ s}^{-1}$ ⁷⁸).

In addition, the time available for the JT-induced reactions leading to H_2 formation is very different from the thermalization time scales. Both t_R and t_N have durations on the order of years. In contrast, the interval between redshifts $z = 1100$ and $z = 1500$ is on the order of 10^5 years. This emphasizes that the thermalization processes under consideration occur on much shorter timescales than the overall cosmic evolution.

This analysis demonstrates that the time required for the hydrogen gas ensemble to reach kinetic energies below 12 cm^{-1} —thereby becoming effectively equivalent to an unconstrained ensemble for three-body reactions—is negligible compared to the timescales for H_2 formation in the early Universe. Consequently, the imposed energy constraint would not alter the probabilities of JT-induced reactions.

Data availability

The datasets generated during and/or analyzed during the study are available from the corresponding author upon reasonable request.

Code availability

MOLPRO software package for electronic structure calculations is publicly available^{57,82}.

Method References

57. Werner, H.-J., Knowles, P. J., Knizia, G., Manby, F. R. & Schütz, M. Molpro: a general-purpose quantum chemistry program package. *WIREs Comput Mol Sci* **2**, 242–253 (2012).
58. Werner, H.-J. & Knowles, P. J. An efficient internally contracted multiconfiguration–reference configuration interaction method. *The Journal of chemical physics* **89**, 5803–5814 (1988).

59. Viegas, L. P., Alijah, A. & Varandas, A. J. Accurate ab initio based multi-sheeted double many-body expansion potential energy surface for the three lowest electronic singlet states of H_3^+ . *The Journal of chemical physics* **126** (2007).
60. Aguado, A., Roncero, O. & Sanz-Sanz, C. Three states global fittings with improved long range: singlet and triplet states of H_3^+ . *Physical Chemistry Chemical Physics* **23**, 7735–7747 (2021).
61. Pandey, A., Vexiau, R., Marcassa, L. G., Dulieu, O. & Bouloufa-Maafa, N. Ultracold charged atom-dimer collisions: State-selective charge exchange and three-body recombination. *Physical Review Research* **6**, 043010 (2024).
62. Cretu, M. T., Mirahmadi, M. & Pérez-Ríos, J. Ion-atom-atom three-body recombination in cold hydrogen and deuterium plasmas. *Physical Review A* **106**, 023316 (2022).
63. Mirahmadi, M. & Pérez-Ríos, J. Ion-atom-atom three-body recombination: From the cold to the thermal regime. *The Journal of Chemical Physics* **158** (2023).
64. Saslaw, W. C. & Zipoy, D. Molecular hydrogen in pre-galactic gas clouds. *Nature* **216**, 976–978 (1967).
65. Peebles, P. & Dicke, R. Origin of the globular star clusters. *Astrophysical Journal, vol. 154, p. 891* **154**, 891 (1968).
66. McDowell, M. On the formation of H_2 in HI regions. *The Observatory, Vol. 81, p. 240-243 (1961)* **81**, 240–243 (1961).
67. Bieniek, R. J. & Dalgarno, A. Associative detachment in collisions of H and H^- . *Astrophysical Journal, Part 1, vol. 228, Mar. 1, 1979, p. 635-639.* **228**, 635–639 (1979).
68. Hirata, C. M. & Padmanabhan, N. Cosmological production of H_2 before the formation of the first galaxies. *Monthly Notices of the Royal Astronomical Society* **372**, 1175–1186 (2006).
69. Sugimura, K., Coppola, C. M., Omukai, K., Galli, D. & Palla, F. Role of the H_2^+ channel in the primordial star formation under strong radiation field and the critical intensity for the supermassive star formation. *Monthly Notices of the Royal Astronomical Society* **456**, 270–277 (2016).
70. Ghosh, S. *et al.* Beyond Born-Oppenheimer theory for ab initio constructed diabatic potential energy surfaces of singlet H_3^+ to study reaction dynamics using coupled 3D time-dependent wave-packet approach. *The Journal of Chemical Physics* **147**, 074105 (2017).

71. Mukherjee, B. *et al.* Beyond Born-Oppenheimer theory for spectroscopic and scattering processes. *International Reviews in Physical Chemistry* **38**, 287–341 (2019).
72. Ghosh, S., Sahoo, T., Baer, M. & Adhikari, S. Charge transfer processes for $\text{H}+\text{H}_2^+$ reaction employing coupled 3D wavepacket approach on beyond Born-Oppenheimer based ab initio constructed diabatic potential energy surfaces. *The Journal of Physical Chemistry A* **125**, 731–745 (2021).
73. Sanz-Sanz, C., Aguado, A. & Roncero, O. Near-resonant effects in the quantum dynamics of the $\text{H} + \text{H}_2^+ \rightarrow \text{H}_2 + \text{H}^+$ charge transfer reaction and isotopic variants. *The Journal of Chemical Physics* **154** (2021).
74. Roncero, O., Andrianarijaona, V., Aguado, A. & Sanz-Sanz, C. Vibrational effects in the quantum dynamics of the $\text{H} + \text{D}_2^+$ charge transfer reaction. *Molecular Physics* **120**, e1948125 (2022).
75. Krstić, P. S. Inelastic processes from vibrationally excited states in slow $\text{H}^+ + \text{H}_2$ and $\text{H} + \text{H}_2^+$ collisions: Excitations and charge transfer. *Physical Review A* **66**, 042717 (2002).
76. Krstić, P. S. Vibrationally resolved collisions in cold hydrogen plasma. *Nuclear Instruments and Methods in Physics Research Section B: Beam Interactions with Materials and Atoms* **241**, 58–62 (2005).
77. Krstić, P., Janev, R. & Schultz, D. Three-body, diatomic association in cold hydrogen plasmas. *Journal of Physics B: Atomic, Molecular and Optical Physics* **36**, L249 (2003).
78. Faure, A., Hily-Blant, P., Pineau des Forêts, G. & Flower, D. The chemistry and excitation of H_2 and HD in the early Universe. *Monthly Notices of the Royal Astronomical Society* **531**, 340–354 (2024).
79. Lykke, K., Murray, K. & Lineberger, W. Threshold photodetachment of H^- . *Physical Review A* **43**, 6104 (1991).
80. Zammit, M. C. *et al.* State-resolved photodissociation and radiative association data for the molecular hydrogen ion. *The Astrophysical Journal* **851**, 64 (2017).
81. Galli, D. & Palla, F. The chemistry of the early Universe. *Astron. Astrophys* **335**, 403–420 (1998).
82. Werner, H.-J. *et al.* The molpro quantum chemistry package. *The Journal of Chemical Physics* **152**, 144107 (2020). URL <https://doi.org/10.1063/5.0005081>.

Acknowledgments We acknowledge E. Roueff (LUX, Observatoire de Paris, France) and S. Charlot (Institut d’Astrophysique de Paris, France) for helpful discussions

and critical comments; we greatly appreciate their input. We also acknowledge support from the Agence Nationale de la Recherche, Grant No. ANR-21-CE30-0060-01 (COCOTRAMOS project) for the primary work on the rubidium system.

Author Contributions A.P., O.D., and N.B. conceived the study of molecular formation via Jahn-Teller-induced coupling. A.P. performed the calculations and led the drafting of the manuscript, with contributions to the text and figures from OD and NB. All authors contributed to the editing and revision of the manuscript.

Competing interests The authors declare no competing interests.

Additional information

Correspondence and requests for materials should be addressed to Amrendra Pandey.